Representing Equilibrium and Nonequilibrium Convection in Large-Scale Models

PETER BECHTOLD, NOUREDDINE SEMANE, AND PHILIPPE LOPEZ

European Centre for Medium-Range Weather Forecasts, Reading, United Kingdom

JEAN-PIERRE CHABOUREAU

Laboratoire d'Aérologie, University of Toulouse and CNRS, Toulouse, France

ANTON BELJAARS AND NIELS BORMANN

European Centre for Medium-Range Weather Forecasts, Reading, United Kingdom

(Manuscript received 5 June 2013, in final form 11 September 2013)

ABSTRACT

A new diagnostic convective closure, which is dependent on convective available potential energy (CAPE), is derived under the quasi-equilibrium assumption for the free troposphere subject to boundary layer forcing. The closure involves a convective adjustment time scale for the free troposphere and a coupling coefficient between the free troposphere and the boundary layer based on different time scales over land and ocean. Earlier studies with the ECMWF Integrated Forecasting System (IFS) have already demonstrated the model's ability to realistically represent tropical convectively coupled waves and synoptic variability with use of the ''standard'' CAPE closure, given realistic entrainment rates.

A comparison of low-resolution seasonal integrations and high-resolution short-range forecasts against complementary satellite and radar data shows that with the extended CAPE closure it is also possible, independent of model resolution and time step, to realistically represent nonequilibrium convection such as the diurnal cycle of convection and the convection tied to advective boundary layers, although representing the late night convection over land remains a challenge. A more in-depth regional analysis of the diurnal cycle and the closure is provided for the continental United States and particularly Africa, including comparison with data from satellites and a cloud-resolving model (CRM). Consequences for global numerical weather prediction (NWP) are not only a better phase representation of convection, but also better forecasts of its spatial distribution and local intensity.

1. Introduction

Equilibrium convection is generally interpreted as indicating that the convection is in equilibrium with the forcing due to the mean advection and processes other than convection. In other words, the convection can react on time scales short enough for the residual tendency between the forcing and the convective stabilization to be small as measured by some function such as the cloud work function or the convective available potential energy (CAPE) (Arakawa and Schubert 1974). This is generally referred to as quasi equilibrium. Numerous theoretical and experimental studies (e.g., Emanuel et al. 1994; Neelin and Yu 1994; Craig 1996; Jones and Randall 2011; Yano and Plant 2012) have confirmed the validity of quasi equilibrium for synoptic disturbances and for time scales of order 1 day. However, various studies (Emanuel 1993; Raymond 1995; Zhang 2002; Donner and Philips 2003; Raymond and Herman 2011) have pointed out that the adjustment in the boundary layer occurs on much shorter time scales than that in the free troposphere.

Today most global numerical weather prediction (NWP) and climate models employ a convection parameterization scheme based on the concept that vertical mass transport occurs in convective plumes that exchange mass with their environment. In these schemes the rate of horizontal mass exchange has to be specified, and the mass flux at cloud base is determined from the

Corresponding author address: Peter Bechtold, European Centre for Medium-Range Weather Forecasts, Shinfield Park, Reading RG2 9AX, United Kingdom.
E-mail: peter.bechtold@ecmwf.int

DOI: 10.1175/JAS-D-13-0163.1

© 2014 American Meteorological Society

assumption of convective quasi equilibrium. A nonexhaustive list of basic parameterization schemes used in these models includes Arakawa and Schubert (1974), Bougeault (1985), Tiedtke (1989), Gregory and Rowntree (1990), Emanuel (1991), Kain and Fritsch (1993), and Zhang and McFarlane (1995), although many of these schemes have later been substantially modified and improved. Despite employing a similar basic convective framework, the models can produce substantially different large-scale tropical wave spectra and intraseasonal variability such as the Madden–Julian oscillation (Lin et al. 2006; Kim et al. 2011; Blackburn et al. 2013; Benedict et al. 2013). However, Bechtold et al. (2008), Vitart and Molteni (2010), Jung et al. (2010), and Hirons et al. (2013a) demonstrated with the European Centre for Medium-Range Weather Forecasts (ECMWF) Integrated Forecasting System (IFS) that the basic mass flux framework under the quasi-equilibrium assumption provides a realistic reproduction of the observed midlatitude synoptic variability, as well as the tropical wave spectra and intraseasonal variability. To achieve this, two important properties of the convection scheme were required: an adaptive adjustment time scale for the CAPE and a realistic strong entrainment rate (Derbyshire et al. 2004; de Rooy et al. 2013). The latter represents the observed heating modes from shallow, congestus, and deep clouds in the tropics (Lin et al. 2012).

In contrast to equilibrium convection, the forcing of nonequilibrium convection varies typically on time scales of a few hours (Jones and Randall 2011; Yano and Plant 2012; Davies et al. 2013). Nonequilibrium convection under rapidly varying forcing typically occurs when either the upper-tropospheric forcing is strong and the convection is inhibited by a capping inversion or the upper-level forcing is weak and the precipitating convection is driven along its trajectory by rapidly varying and strong surface heat fluxes. Note that the quasigeostrophic adjustment process of a net heat source occurs via inertia–gravity waves on time scales of a few hours. Forecasting nonequilibrium convection is challenging for models, and this is particularly true for surface-forced convection where the mesoscale adiabatic lifting–sinking couplet in the free troposphere is the response to and not the source of convective heating.

The diurnal cycle of convection is probably the most prominent manifestation of nonequilibrium convection driven by the boundary layer. Numerous observational studies (e.g., Yang and Slingo 2001; Dai et al. 1999; Tian et al. 2005; Zhang and Klein 2010) and those based on cloud-resolving models (CRMs) (e.g., Chaboureau et al. 2004; Khairoutdinov and Randall 2006; Schlemmer et al. 2011) have been devoted to the diurnal cycle of convection over land. The phase of the diurnal cycle can strongly vary on regional scales, although the general picture is that of a morning shallow convective phase, followed by a gradual onset of deeper convection, with rain rates peaking in the late afternoon to early evening. It has been found that the phase and intensity of precipitation mainly depend on the surface fluxes and lower- to midtropospheric stability and moisture, but boundary layer processes such as convergence, gravity waves, and cold pools also play a role in the onset and propagation of deep convection. It has been shown that CRMs with resolutions of order 2.5 km or higher are able to reproduce the observed diurnal cycle (e.g., Petch et al. 2002; Sato et al. 2008; Stirling and Stratton 2012), but a strong resolution sensitivity exists with respect to both amplitude and phase for coarser horizontal resolutions when no convection parameterization is employed. However, Sato et al. (2009) and Marsham et al. (2013) have reasonably reproduced the observed phase in CRM-type simulations at 7- and 12-km horizontal resolutions, respectively.

The same success in reproducing the observed diurnal cycle can generally not be reported for large-scale models. Indeed, numerous global and regional model studies (Slingo et al. 1992; Dai et al. 1999; Betts and Jakob 2002; Bechtold et al. 2004; Clark et al. 2007; Brockhaus et al. 2008; Stratton and Stirling 2012; Langhans et al. 2013; Marsham et al. 2013) and comparisons of CRMs with single-column models (Guichard et al. 2004; Grabowski et al. 2006) pointed to systematic errors in the diurnal cycle of precipitation when a convection parameterization scheme is employed, namely a too-early onset of deep convection with a diurnal cycle of precipitation that is roughly in phase with the surface fluxes. A notable exception is the successful simulations reported by Takayabu and Kimoto (2008). The diurnal cycle of nonprecipitating shallow convection, however, can be realistically represented with a quasi-equilibrium closure for the boundary layer and a prognostic cloud scheme, as demonstrated with the IFS by Ahlgrimm and Forbes (2012).

Various approaches have been taken to improve the representation of convection driven by surface fluxes. While Piriou et al. (2007), Del Genio and Wu (2010), and Stratton and Stirling (2012) focused on the entrainment rates, important work has also been done on convective closure as reviewed in Yano et al. (2013). In particular, Pan and Randall (1998) and Gerard et al. (2009) accounted for convective memory through a prognostic closure for the updraft kinetic energy and/or updraft area fraction. Mapes (2000), Rio et al. (2009), and Fletcher and Bretherton (2010) proposed convective closures involving the convective inhibition (CIN) and/or lifting by cold pools, while a humidity-dependent

closure has been adopted in Fuchs and Raymond (2007). However, so far none of the above methods have proved to be general and robust enough to replace, at least in the global NWP context, the standard equilibrium closures for the CAPE or cloud work function. The notable exception is the studies by Donner and Philips (2003) and Zhang (2002), who evaluated the quasi-equilibrium assumption for CAPE against observations, while recognizing findings by Raymond (1995) on different adjustment time scales for the free troposphere and the boundary layer. From those studies, it was concluded that it should be possible to formulate a CAPE closure for the free troposphere under a quasi-equilibrium assumption that also holds for rapidly varying boundary layer forcing.

The above considerations constitute the basis for the present article, where we derive a CAPE closure involving appropriate boundary layer time scales over land and water. Indeed, we show that with this extended diagnostic closure it is possible to represent not only large-scale synoptically driven convection, but also nonequilibrium boundary layer–driven convection with its characteristic diurnal cycle, and the inland advection of wintry convective showers. The article is organized as follows. The CAPE closure is derived in section 2, followed in section 3 by an evaluation against satellite and radar data of the diurnal cycle of convection in low-resolution seasonal integrations and high-resolution short-range forecasts. A more in-depth discussion of the physics of the new closure and the diurnal cycle in the Sahel region, which makes use of complementary satellite and CRM data, is provided in section 4. Conclusions and consequences for NWP are discussed in section 5, including a brief discussion of a wintry convective situation under strong advection.

2. Convective closures

The convective available potential energy CAPE ($\mathrm{J\,kg^{-1}}$) is defined as the buoyancy integral,

$$\mathrm{CAPE} = g\int_{z_{\mathrm{base}}}^{z_{\mathrm{top}}} \frac{T_v^{\mathrm{upad}} - \overline{T}_v}{\overline{T}_v}\,dz \approx g\int_{z_{\mathrm{base}}}^{z_{\mathrm{top}}} \frac{\theta_e^{\mathrm{upad}}(T,q) - \theta_{e\mathrm{sat}}(\overline{T})}{\theta_{e\mathrm{sat}}(\overline{T})}\,dz, \qquad (1)$$

where the integration in height coordinates z is between cloud base and cloud top, T_v is the virtual temperature, and g is gravity; the superscript "upad" denotes values of an air parcel lifted pseudoadiabatically, (i.e., without considering mixing with environmental air), and overbars denote environmental or grid-mean values. For diagnostic purposes CAPE can be reasonably approximated by using the saturated equivalent potential temperature $\theta_{e\mathrm{sat}}$ instead of $\overline{T}_v$, and the equivalent potential temperature θ_e^{upad}, depending on temperature T and specific humidity q, instead of T_v^{upad}. As θ_e is conserved during moist adiabatic ascent, the rhs of (1) shows that the updraft thermodynamic properties are determined by the temperature and moisture in the departure layer of the rising air parcel that predominantly roots in the boundary layer.

In the context of convection parameterization we use integration over pressure and define PCAPE ($\mathrm{J\,m^{-3}}$) as the density-weighted buoyancy integral of an entraining ascending air parcel:

$$\mathrm{PCAPE} = -\int_{p_{\mathrm{base}}}^{p_{\mathrm{top}}} \frac{T_v^{\mathrm{up}} - \overline{T}_v}{\overline{T}_v}\,dp. \qquad (2)$$

The entrainment rates used to compute T_v^{up} are given in the appendix. The advantage of PCAPE over an entraining CAPE is the density scaling that more readily relates the time derivative of PCAPE to the convective mass flux.

Under the assumption of vanishing updraft temperature excess at cloud top, and using $T_v^{\mathrm{up}} - \overline{T}_v \ll \overline{T}_v$, the time derivative of PCAPE is obtained as

$$\frac{\partial \mathrm{PCAPE}}{\partial t} = \underbrace{\int_{p_{\mathrm{base}}}^{p_{\mathrm{top}}} \frac{1}{\overline{T}_v}\frac{\partial \overline{T}_v}{\partial t}\,dp}_{\mathrm{LS+CONV}} - \underbrace{\int_{p_{\mathrm{base}}}^{p_{\mathrm{top}}} \frac{1}{\overline{T}_v}\frac{\partial T_v^{\mathrm{up}}}{\partial t}\,dp + \left.\frac{T_v^{\mathrm{up}} - \overline{T}_v}{\overline{T}_v}\right|_{\mathrm{base}} \frac{\partial p_{\mathrm{base}}}{\partial t}}_{\mathrm{BL+CONV}}. \qquad (3)$$

The evolution of PCAPE includes production of PCAPE by radiative and advective large-scale processes (LS), and destruction of PCAPE by cumulus convection (CONV), both affecting $\overline{T}_v$. Furthermore, there is production of PCAPE by boundary layer (BL) processes other than convection, and removal by convective boundary layer venting, and cooling by downdrafts and subcloud rain evaporation, all affecting T_v^{up}. The prognostic equation for PCAPE can then be formally rewritten as

$$\frac{\partial \mathrm{PCAPE}}{\partial t} = \left.\frac{\partial \mathrm{PCAPE}}{\partial t}\right|_{\mathrm{LS}} + \left.\frac{\partial \mathrm{PCAPE}}{\partial t}\right|_{\mathrm{BL}} + \left.\frac{\partial \mathrm{PCAPE}}{\partial t}\right|_{\mathrm{CONV=shal+deep}}. \quad (4)$$

Note that the CONV term contains both the convective stabilization of the free troposphere (LS) and the boundary layer (BL); it is the sum of the contributions from shallow and deep convection.

Similar prognostic equations for CAPE have also been derived in Zhang (2002) and Donner and Philips (2003).

The LS production term includes the tendencies due to mean vertical and horizontal advection and radiation. It is given by

$$\left.\frac{\partial \mathrm{PCAPE}}{\partial t}\right|_{\mathrm{LS}} = \int_{p_{\mathrm{base}}}^{p_{\mathrm{top}}} \frac{1}{\overline{T}_v} \left.\frac{\partial \overline{T}_v}{\partial t}\right|_{\mathrm{adv+rad}} dp. \quad (5)$$

The tendency due to convection can either be approximated assuming that cumulus convection acts to remove PCAPE over a convective time scale τ (Fritsch and Chappell 1980; Betts and Miller 1986; Nordeng 1994)

$$\left.\frac{\partial \mathrm{PCAPE}}{\partial t}\right|_{\mathrm{CONV},1} = -\frac{\mathrm{PCAPE}}{\tau}, \quad (6)$$

or by approximating the convective tendency by the heating through compensating environmental subsidence, so that the convective mass flux M ($\mathrm{kg\,m^{-2}\,s^{-1}}$) becomes apparent

$$\left.\frac{\partial \mathrm{PCAPE}}{\partial t}\right|_{\mathrm{CONV},2} \approx -\int_{z_{\mathrm{base}}}^{z_{\mathrm{top}}} \frac{g}{\overline{T}_v} M \left(\frac{\partial \overline{T}_v}{\partial z} + \frac{g}{c_p}\right) dz = -\frac{M_{\mathrm{base}}}{M^*_{\mathrm{base}}} \int_{z_{\mathrm{base}}}^{z_{\mathrm{top}}} \frac{g}{\overline{T}_v} M^* \left(\frac{\partial \overline{T}_v}{\partial z} + \frac{g}{c_p}\right) dz, \quad (7)$$

with c_p being the specific heat at constant pressure. The ratio between the actual (final) cloud-base mass flux and the unit (initial) cloud-base mass flux ($M_{\mathrm{base}}/M^*_{\mathrm{base}}$) is the convective scaling or closure factor. The initial mass flux profile M^* and initial cloud-base mass flux M^*_{base} are known from the updraft computation.

Different convective closures can then be formulated on the basis of (4), keeping in mind that a mass flux scheme requires a closed expression for M_{base}, and therefore we need to retain (7). If we know the BL term, PCAPE can be determined prognostically from (4) using (5) and (6). The convective mass flux is then obtained diagnostically from

$$\left.\frac{\partial \mathrm{PCAPE}}{\partial t}\right|_{\mathrm{CONV},2} = \left.\frac{\partial \mathrm{PCAPE}}{\partial t}\right|_{\mathrm{CONV},1}. \quad (8)$$

Alternatively, in a purely diagnostic scheme we can compute PCAPE from (2), and again use (8) to compute the convective mass flux. Note that in this diagnostic formulation PCAPE implicitly contains the production from BL and LS.

Another diagnostic closure is obtained from (4) if we use (5) and (7), neglect the lhs, and assume a boundary layer in equilibrium:

$$\left.\frac{\partial \mathrm{PCAPE}}{\partial t}\right|_{\mathrm{LS}} = -\left.\frac{\partial \mathrm{PCAPE}}{\partial t}\right|_{\mathrm{CONV},2}. \quad (9)$$

This relation is another formulation of the quasi-equilibrium between the large-scale destabilization and the convection but, as defined by the integral bounds, it is the quasi equilibrium for the free troposphere. No τ has to be specified, as it is implicitly contained in the LS tendency. However, experimentation shows that this closure is not general enough, as it underestimates convective activity in situations where the LS forcing is weak, and where convective heating precedes the dynamic adjustment.

Finally, even a suitable moisture convergence closure can be formulated that is consistent with (4) using (7):

$$\int_{p_{\mathrm{surf}}}^{p_{\mathrm{top}}} \left.\frac{\partial \overline{q}}{\partial t}\right|_{\mathrm{adv+BL}} dp = \left.\frac{\partial \mathrm{PCAPE}}{\partial t}\right|_{\mathrm{CONV},2}, \quad (10)$$

where the integration is from the surface to the top of the atmosphere including LS and BL. This closure, despite assuming moisture as a source of convection instead of instability, has properties of both (9) and (8). It is still applied in NWP (Bougeault 1985), but tests with the IFS did not lead to optimal model performance.

a. Diagnostic CAPE closure

As outlined above, a convenient diagnostic CAPE closure can be defined using (8) and substituting for (7) and (6) and computing PCAPE from (2). The cloud-base mass flux is then obtained as

$$M_{\mathrm{base}} = M^*_{\mathrm{base}} \frac{\mathrm{PCAPE}}{\tau} \frac{1}{\int_{z_{\mathrm{base}}}^{z_{\mathrm{top}}} (g/\overline{T}_v) M^* (\partial \overline{T}_v/\partial z + g/c_p)\, dz}. \quad (11)$$

Apart from using a density-weighted PCAPE instead of an entraining CAPE, this is the closure for the deep convective mass fluxes that has been used in the IFS since Gregory et al. (2000). With this formulation the convective mass flux closely follows the large-scale forcing and/or the surface fluxes when the CIN is small and the adjustment time scale is reasonably short.

The closure in (11) is complete with a definition of the convective adjustment time scale following Bechtold et al. (2008):

$$\tau = \frac{H_c}{\overline{w}^{\mathrm{up}}} f(n) = \tau_c f(n); \quad f(n) = 1 + \frac{264}{n}. \tag{12}$$

Here, τ_c is the convective turnover time scale, H_c is the convective cloud depth, $\overline{w}^{\mathrm{up}}$ is the vertically averaged updraft velocity, and f is an empirical scaling function decreasing with increasing spectral truncation (horizontal resolution) n. The minimum allowed value for τ is set to 12 min. Note that τ_c depends itself on PCAPE through $\overline{w}^{\mathrm{up}}$, which is consistent with the observations by Zimmer et al. (2011). In the following the closure described by (11) and (12) is referred to as CTL.

b. *Diagnostic CAPE closure with boundary layer equilibrium*

As the above the closure in (11) does not reproduce the observed diurnal cycle (as shown later), even when employing large entrainment rates in the convection scheme that are consistent with CRM data (Del Genio and Wu 2010; de Rooy et al. 2013), it is suggested that it does not reproduce the observed nonequilibrium between the boundary layer forcing and the deep convection. Zhang (2002) and Donner and Philips (2003) have shown through an analysis of observational data of midlatitude and tropical convection that the assumption that $\partial\mathrm{PCAPE}/\partial t$ is small compared to the individual terms on the rhs of (4) is not valid if the boundary layer is not in equilibrium. Indeed the boundary layer production term is the dominant term in surface-driven convection under weak large-scale forcing. To our knowledge, in most parameterizations using a CAPE-type closure, the imbalance between the deep convection and the BL production is not explicitly taken into account. However, some authors (e.g., Raymond 1995) have taken an alternative approach by proposing separate boundary layer equilibrium closures.

We define the total boundary layer production in (4) as proportional to the surface buoyancy flux:

$$\left.\frac{\partial \mathrm{PCAPE}}{\partial t}\right|_{\mathrm{BL}} = -\frac{1}{T_\star}\int_{p_{\mathrm{surf}}}^{p_{\mathrm{base}}} \left.\frac{\partial \overline{T}_v}{\partial t}\right|_{\mathrm{BL}} dp, \tag{13}$$

where $\partial\overline{T}_v/\partial t|_{\mathrm{BL}}$ includes the tendencies from mean advection, diffusive heat transport, and radiation. In the model context these tendencies must be available before the convection is taken into account. The temperature $T_\star$ scales as $T_\star = c_p^{-1} gH$, with H being a characteristic height. We have set $T_\star = 1$ K and cast the scaling into the coefficient α below. In a prognostic scheme one could in principle formulate the boundary layer contribution to be formally consistent with the second term on the rhs of (3), the third term being generally small. However, the BL contribution in (3) is the sum of the convective contribution and the forcing. In a model, the nonconvective BL forcing could be isolated, by calculating the BL temperature tendency due to nonconvective terms. Furthermore, the tendency of the updraft virtual temperature can be rather discontinuous in space and time, and even become negative while there is surface heating. Therefore, (13) is the preferred formulation of the boundary layer contribution to PCAPE taking into account all relevant forcings.

To account for the imbalance between boundary layer heating and deep convective overturning, we write the convective tendency as the relaxation of an effective PCAPE:

$$\left.\frac{\partial \mathrm{PCAPE}}{\partial t}\right|_{\mathrm{CONV=deep}} = -\frac{\mathrm{PCAPE}}{\tau} + \alpha \left.\frac{\partial \mathrm{PCAPE}}{\partial t}\right|_{\mathrm{BL}}; \quad \alpha = \frac{\tau_{\mathrm{BL}}}{\tau}, \tag{14}$$

with α being the fraction of boundary layer forcing consumed by shallow convection. Note that α is given as the ratio of the boundary layer time scale τ_{BL} to the deep convective adjustment time scale τ and can also be interpreted as a convective coupling coefficient between the free troposphere and the boundary layer, with $\alpha = 0$ corresponding to a perfect coupling regime and $\alpha = 1$ to decoupling. The boundary layer time scale should satisfy the dimensional form $[HU_\star^{-1}]$, where $U_\star$ is a characteristic speed. It is set equal to τ_c over land, assuming that the boundary layer adjusts to deep convective heat transport through the updrafts and downdrafts. Over water it is set to the horizontal advective time scale, assuming a quasi-homogeneous oceanic boundary layer in equilibrium:

$$\begin{aligned} \tau_{\mathrm{BL}} &= \tau_c \quad \text{over land,} \\ \tau_{\mathrm{BL}} &= \frac{H_{\mathrm{base}}}{\overline{u}_{\mathrm{BL}}} \quad \text{over water,} \end{aligned} \tag{15}$$

where H_{base} is the cloud-base height and $\overline{u}_{\mathrm{BL}}$ is the average horizontal wind speed in the subcloud layer.

Setting $\partial\mathrm{PCAPE}/\partial t = 0$ in (4) enforces essentially a balance between the second and third term on the rhs when the boundary layer forcing dominates, and an equilibrium between the first and third term, when the boundary layer is in equilibrium and the large-scale

forcing dominates. Using (14) for the PCAPE consumption by deep convection and following the same procedure as used for deriving (11), the scaling for the deep convective cloud-base mass flux can be written as

$$M_{\rm base} = M^*_{\rm base}\frac{\rm PCAPE - PCAPE_{BL}}{\tau}\frac{1}{\int_{z_{\rm base}}^{z_{\rm top}} (g/\overline{T}_v)M^*(\partial\overline{T}_v/\partial z + g/c_p)\,dz}; \quad M_{\rm base} \geq 0, \tag{16}$$

with

$$\rm PCAPE_{BL} = -\tau_{BL}\frac{1}{T_\star}\int_{p_{surf}}^{p_{base}}\left.\frac{\partial\overline{T}_v}{\partial t}\right|_{\rm BL} dp \tag{17}$$

for convection rooting in the boundary layer. For convection rooting above the boundary layer, $\rm PCAPE_{BL}$ is set to zero. The closure is equivalent to relaxing PCAPE toward a value $\rm PCAPE_{BL}$ instead of zero. It considers only the part of PCAPE that is due to free-tropospheric production as long as the boundary layer is not in equilibrium. The closure consists of subtracting from the total mass flux a (time dependent) fraction of the shallow convective contribution (see below) that is supposed to approximately balance the boundary layer heat and moisture fluxes. The closure might also be interpreted as providing a correction to the prediction of convective ensemble properties (mass flux) by simple parcel theory (CAPE). Importantly, the different factors in (16) mutually interact, and it will be shown that when integrated over a diurnal cycle (16) roughly produces the same daily averaged mass flux and precipitation as (11). The scaling (17) is consistent with the free-tropospheric and energy conversion scaling suggested in Shutts and Gray (1999), when using the surface buoyancy flux instead of the integrated tendencies. In the following the closure specified by (16) is referred to as NEW.

c. Closure for shallow convection

A distinction between deep and shallow convection is made on the basis of the first-guess convective cloud depth. If the cloud extends over more than 200 hPa then convection is classified as deep, and shallow otherwise. This distinction is only necessary for the closure and the specification of the entrainment rates that are a factor of 2 larger for shallow convection (see the appendix). In the case of very shallow convection both PCAPE and the denominator in (16) tend to zero, and a closure based solely on boundary layer equilibrium becomes appropriate. A closure for shallow convection is obtained by assuming a balance between the second and third terms on the rhs of (4) (i.e., a balance between the convection and the mean advection and other physical processes in the boundary layer), and replacing the tendency for PCAPE by the vertically integrated tendency of the moist static energy h:

$$\int_{p_{surf}}^{p_{base}}\left.\frac{\partial\overline{h}}{\partial t}\right|_{\rm CONV} dp = g|_{p_{surf}}^{p_{base}}F_h = -\int_{p_{surf}}^{p_{base}}\left.\frac{\partial\overline{h}}{\partial t}\right|_{\rm BL} dp, \tag{18}$$

where F_h is the convective moist static energy flux. Assuming zero convective mass flux at the surface, the cloud-base mass flux is then obtained as

$$M_{\rm base}(h^{\rm up}_{\rm base} - \overline{h}_{\rm base}) = -\frac{1}{g}\int_{p_{surf}}^{p_{base}}\left.\frac{\partial\overline{h}}{\partial t}\right|_{\rm BL} dp; \quad M_{\rm base} \geq 0. \tag{19}$$

The deep and shallow convective closures in (11), (16), and (19) together with the entrainment/detrainment rates in (A1)–(A3) take into account the vertical stratification and/or the boundary layer tendencies. Together with the horizontally variable time scales τ_c, and $\tau_{\rm BL}$, the closures provide a flexible framework so that the convective fluxes can adjust to varying synoptic and boundary conditions.

3. Diurnal cycle of precipitation

a. Climatology

The diurnal cycle of convection in the IFS is first evaluated from an ensemble of 1-yr integrations and compared against a 10-yr precipitation climatology from the Tropical Rainfall Measuring Mission (TRMM) (Nesbitt and Zipser 2003; Takayabu and Kimoto 2008). The simulations are forced by analyzed sea surface temperatures, and use spectral truncation $n = 159$ ($\Delta x =$ 125 km) with 91 vertical levels, and a time step of 1 h. Precipitation data from both the simulations and the observations are composited in hourly bins, and the diurnal amplitude and phase are computed from the first harmonic of a Fourier series.

The diurnal amplitude (mm day^{-1}) of the precipitation in the tropical belt from the TRMM radiometer is displayed in Fig. 1a. Maximum amplitudes reach around 10 mm day^{-1} over tropical land. Amplitudes from the

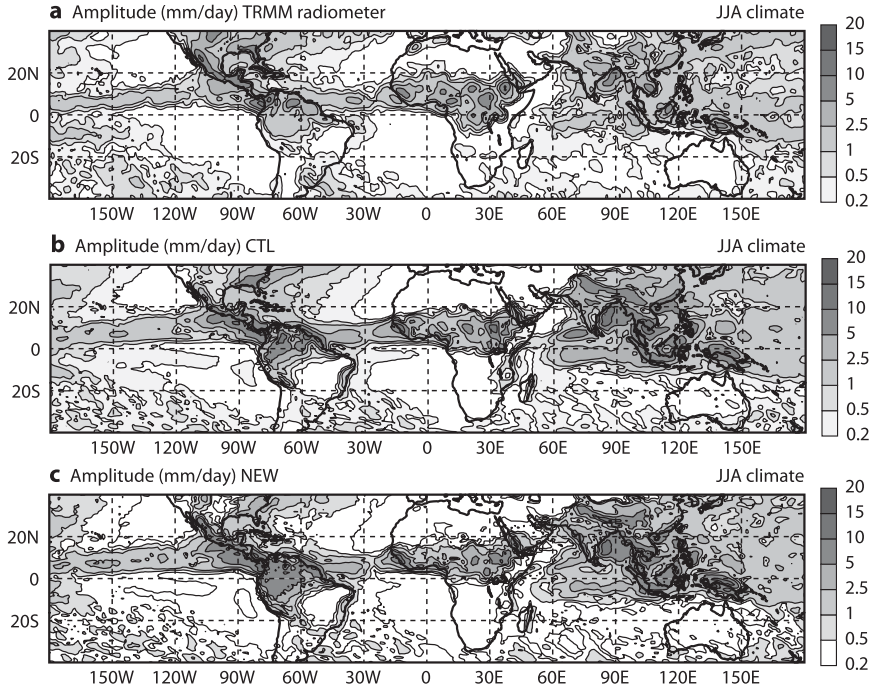

FIG. 1. Diurnal amplitude (mm day^{-1}) of the precipitation in the tropical band as obtained (a) from a 10-yr climatology of TRMM radiometer data (courtesy of Yukari Takayabu and colleagues), and from an ensemble of annual IFS integrations at truncation $n = 159$ ($\Delta x = 125$ km) with (b) CTL and (c) NEW closure.

model integrations using the CTL and NEW closures are displayed in Figs. 1b and 1c. Overall, the spatial distribution of the amplitudes is reasonably reproduced in the simulations, but the amplitudes reach higher values, particularly over northern Amazonia. However, the simulated total rainfall over Amazonia appears realistic when compared to the Global Precipitation Climatology Project (GPCP) 2.2 dataset (not shown).

The corresponding phase of the diurnal cycle (LST) is displayed in Fig. 2. As already discussed in earlier studies, maximum precipitation in the TRMM radar data (Fig. 2a) occurs over tropical land roughly in the late afternoon to early evening, although strong regional variations are present. In particular, in the TRMM climatology convective rainfall over Amazonia occurs during the early afternoon but may peak as early as local noon due to the high relative humidity and low stability in the lower troposphere (Betts and Jakob 2002). In contrast, maximum precipitation over the tropical oceans occurs during the early morning. The CTL (Fig. 2b) provides a reasonable reproduction of the diurnal phase over water, but the convective precipitation over land generally peaks around local noon, except over Amazonia where it peaks during late morning. This systematic model error has not improved significantly in the IFS over the last decades (Slingo et al. 1992; Bechtold et al. 2004). However, a marked improvement is obtained with the NEW closure that shifts the diurnal cycle over land by 4–5 h compared to CTL and also improves the diurnal cycle in coastal regions, (e.g., off the Central American and West African coasts, as well as off the Indian subcontinent, and over the Maritime Continent). Experimentation shows that the improvements over coastal regions are primarily due to a better representation of the convection generated over land and advected over sea, along with the associated subsiding motions, but the modified adjustment over sea via τ_{BL} also contributes.

b. High-resolution integrations

In addition to seasonal integrations, higher-resolution daily 3-day forecasts have been performed for June–August (JJA) 2011 and 2012 using $n = 511$ ($\Delta x = 40$ km) with 137 vertical levels and a time step of 900 s. The forecasts were initialized from ECMWF's operational analyses at $n = 1279$ ($\Delta x = 16$ km) with 91 levels. The forecasts are compared to the National Centers for Environmental Prediction (NCEP) stage IV composites (Lin and Mitchell 2005) obtained from the combination of radar and rain gauge data (NEXRAD hereafter) over the continental United States during summer 2011 and 2012, and German radar composites from the Deutsche

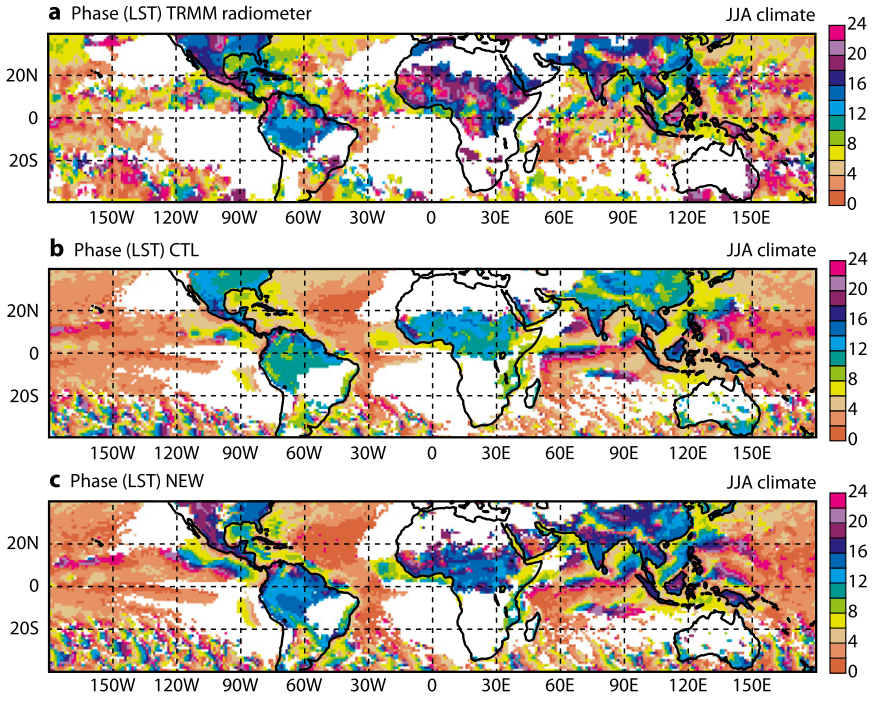

FIG. 2. As in Fig. 1, but for the diurnal phase (LST) of the precipitation. Also TRMM radar data have been used instead of the radiometer data. White shading is applied for areas where the amplitude of precipitation is below 0.2 mm day^{-1}.

Wetterdienst for summer 2011. All forecast days have been used to compute the diurnal composites, that is, 3×90 days for each JJA season.

The amplitude and phase of the diurnal cycle of precipitation averaged over the summers 2011 and 2012 are depicted in Figs. 3 and 4 for the continental United States. Numerous previous studies have already described the diurnal cycle over this region (e.g., Dai et al. 1999; Tian et al. 2005). In summary, as is also evident from the NEXRAD data (Figs. 3a and 4a), the diurnal cycle over the continental United States is characterized by three distinctive regions: the Rocky Mountains area, where convective activity peaks during the late afternoon, the Central Plains with predominantly nighttime convection from propagating mesoscale convective systems triggered over the Rocky Mountains, and the eastern United States and coastal regions with predominantly late afternoon convection and a particularly strong diurnal amplitude over the Florida peninsula.

The CTL forecasts have quite a reasonable representation of the spatial variations in the amplitude (Fig. 3b) but underestimate the amplitude east of the mountain ridge and somewhat overestimate the amplitude in the coastal regions. The results with the NEW forecasts are rather similar although they slightly improve on the CTL. However, concerning the phase (Fig. 4) the NEW forecasts substantially delay the diurnal cycle by 4–5 h compared to CTL so that the results more closely match the observations, although over the eastern United States the diurnal cycle in NEW still precedes the observed cycle by up to 2 h.

To give an overview of the diurnal cycle in the high-resolution short-range forecasts, the area-averaged diurnal rainfall composites are depicted in Fig. 5 for the eastern United States and Germany and also for the central Sahel region, which has TRMM climatological data for comparison. The area-averaged representation shows that NEW has quite a good fit to the daytime and evening diurnal cycle of precipitation, shifting it by up to 6 h compared to CTL. The late night precipitation, however, remains underestimated in both NEW and CTL despite having the convection parameterization coupled to a five-species prognostic cloud scheme via the detrainment of convective condensate. The late night precipitation deficit might be due to the missing representation of convective system dynamics including spreading surface cold pools and predominantly upper-level mesoscale lifting during the night. Finally, over the Sahel (Fig. 5c), NEW realistically increases the precipitation with respect to CTL. As shown by Marsham et al. (2013), a correct phase representation of the diurnal cycle is particularly important in this region where

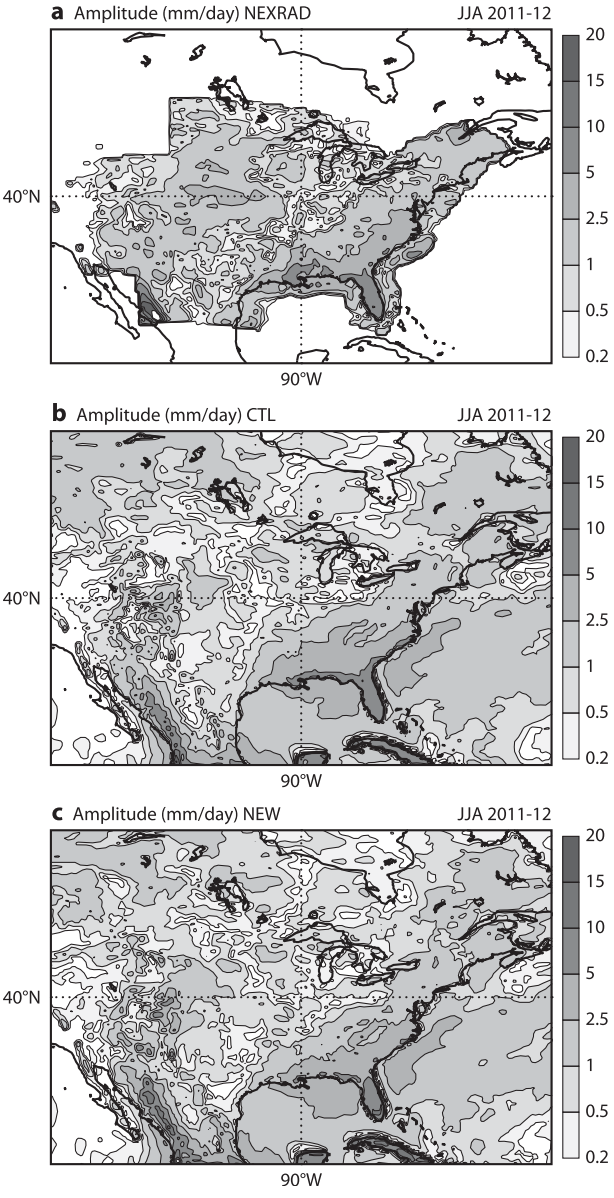

FIG. 3. Amplitude (mm day^{-1}) of the precipitation averaged over JJA 2011 and 2012 for the continental United States from (a) NEXRAD, and from daily 72-h forecasts at truncation n = 511 (Δx = 40 km) with (b) CTL and (c) NEW closure. The RMSE against observations does not differ significantly between CTL and NEW.

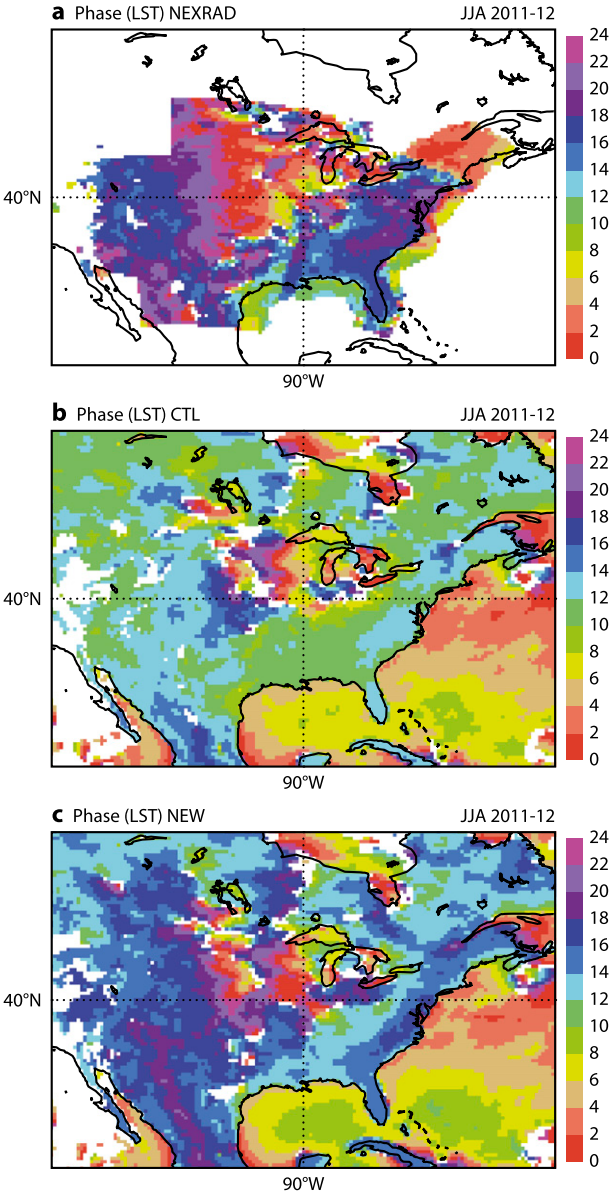

FIG. 4. As in Fig. 3, but for the diurnal phase of the precipitation (LST).

the convective heating is a key driver of the meridional pressure gradient and the large-scale dynamics.

4. Discussion

In the following we focus on the central Sahel region (as defined in Fig. 5c) for the analysis of the convective closure and also provide further evaluation of the convective heating and its dynamical response using CRM and complementary satellite data. All model results are based on the high-resolution short-range forecasts discussed in the previous section. In addition to the forecasts, data assimilation cycles have been run with the IFS, providing a more direct comparison of model and data in space and time. The CRM data are from the Meso-NH limited-area model (Lafore et al. 1998) that has been run during 10–25 June 2012 at 2.5-km grid spacing daily for 24 h over the central Sahel region (i.e., roughly a 2200 km × 1700 km large domain). The CRM uses the same ECMWF n = 1279 analyses as initial conditions as are used for CTL and NEW. In addition,

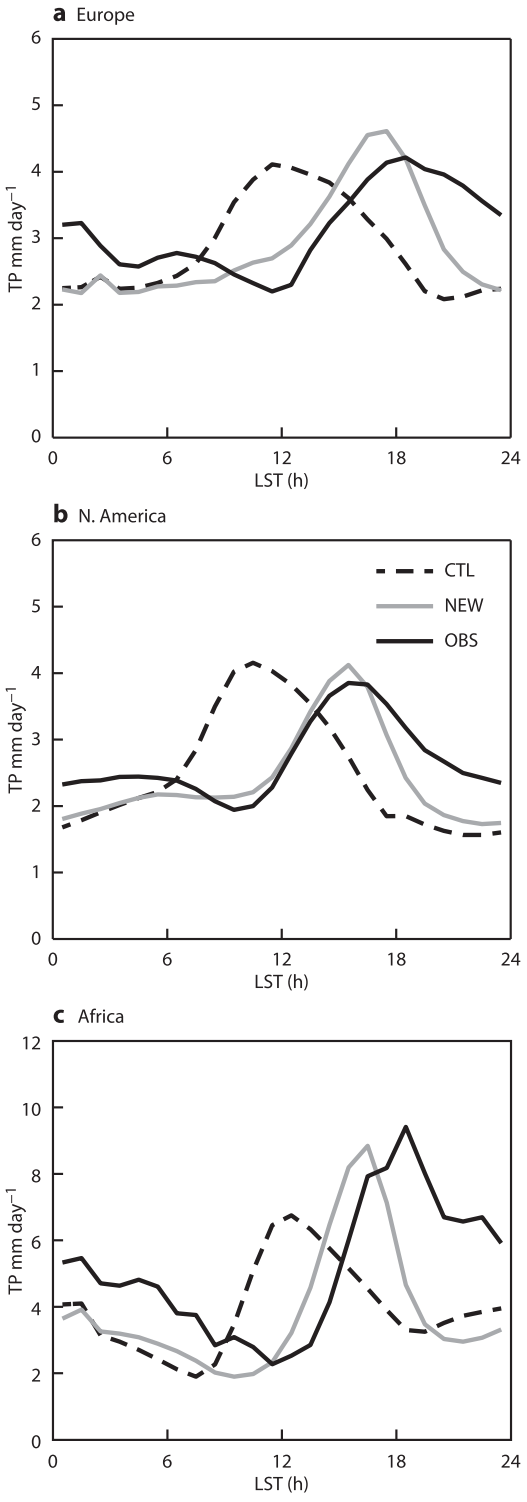

FIG. 5. Diurnal composites of area-averaged total precipitation (mm day^{-1}) from CTL (black solid lines) and NEW (dashed lines) against observations for JJA 2011 (Europe) and JJA 2011 and 2012 for the other areas: (a) Germany (48°–52°N, 7°–14°E) using DWD radar, (b) the eastern United States (30°–45°N, 100°–80°W) using NEXRAD, and (c) the central Sahel region (5°–20°N, 10°–30°E) using TRMM climatological radiometer data.

the CRM open boundaries are updated every 6 h from the analyses.

a. Diagnostics on closure

Diurnal composites of quantities related to the convective closure are illustrated in Fig. 6 for the period 10–25 June 2012; shown are the total-area averages (dashed lines) and averages only over the convectively active grid columns (solid lines), which are also labeled by the suffix "c" (for convective). The quantities considered in Fig. 6 include the surface convective precipitation rate, the CAPE in (1), and the various terms involved in the closures in (11) and (16): (a) the cloud-base convective mass flux; (b) PCAPE′, which takes the value of PCAPE in CTL and the value of PCAPE − PCAPE_{BL} in NEW; (c) the convective adjustment time scale in (12); and (d) the stabilization by compensating subsidence in (7). The surface convective precipitation rate is proportional to the convective mass flux at cloud base times the updraft rain/snow content, although over land it is also strongly affected by evaporation in the subcloud layer. It is also approximately equal to the total surface precipitation as most stratiform precipitation evaporates before reaching the ground.

Concerning the total area averages, one notices that for both CTL and NEW the convective precipitation, mass flux, and PCAPE′ are in phase. The forecasts barely differ during night, but there is a clear 5-h shift in the maxima in NEW with respect to CTL. CAPE (Fig. 6b) has been computed diagnostically for all grid columns from the mean thermodynamic profiles, while PCAPE is computed inside the convection scheme and therefore is nonzero only in grid columns with active convection. CAPE has much larger values than PCAPE, reflecting the importance of entrainment. The main conclusion here is that CAPE shows an unphysical maximum at 1000 LST in CTL, if taken as either a domain average or averaged over the convective regions, while its evolution in NEW roughly follows the evolution of the surface heat fluxes.

The evolution of the convective area averages CTLc, NEWc, and CRMc (solid lines) is more revealing. Note that the cloud-base mass flux (or convective precipitation) is proportional to PCAPE′/τ divided by the subsidence term. In CTLc most closure-related quantities peak around 1000 LST, vary only weakly during daytime, and precede the peak in domain-mean mass flux and precipitation by about 2 h. In contrast, the daytime amplitudes are important in NEWc, and the total domain and convective domain averages are in phase. It will be shown later that the reason for this is that the convection in NEW is strongest at the end of the lower-tropospheric moistening phase, while in CTL

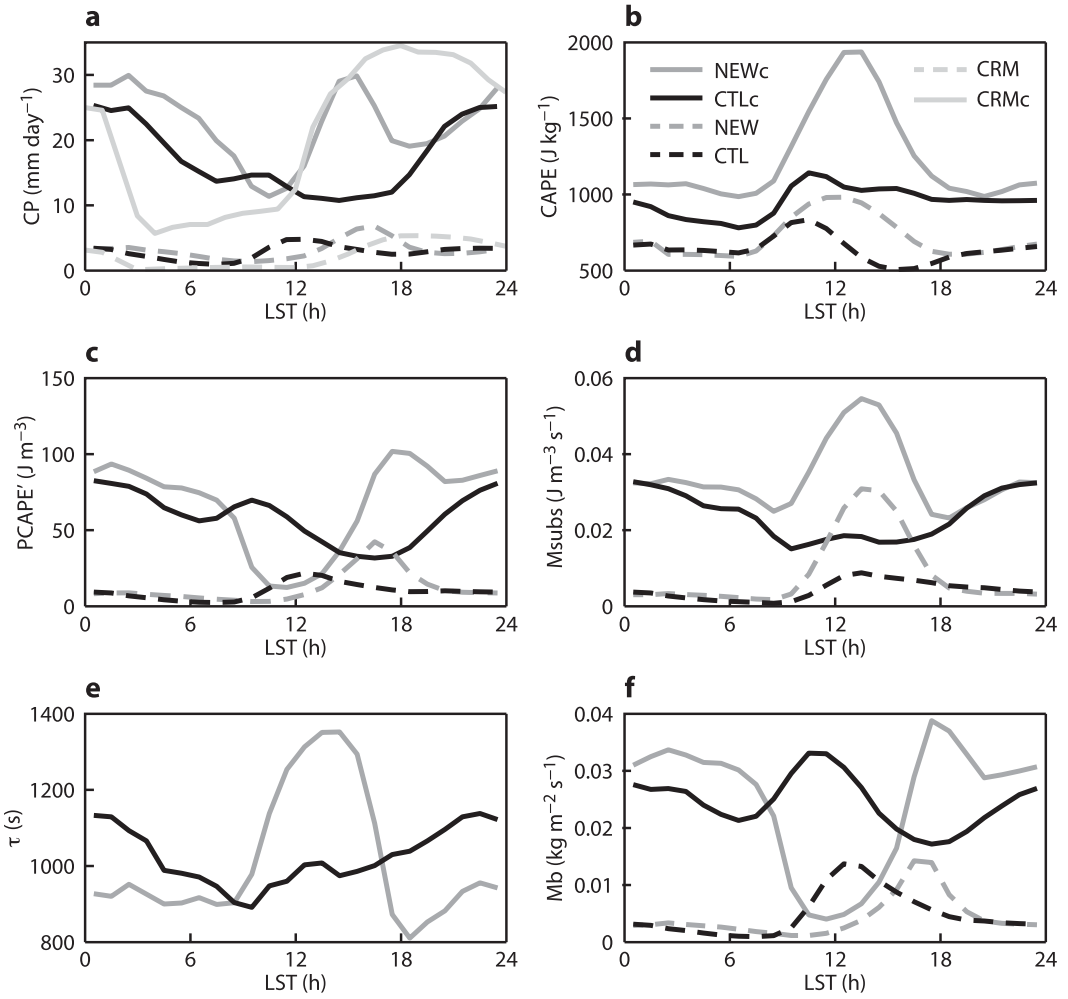

FIG. 6. Diurnal composites of convective closure–related diagnostics during 10–25 Jun 2012 over the central Sahel region: (a) Convective precipitation, (b) CAPE, (c) PCAPE′ = PCAPE for CTL and PCAPE − PCAPE_{BL} for NEW, (d) the compensating mass flux term in (5), (e) the convective adjustment time scale, and (f) the cloud-base mass flux. Dashed lines denote total-area averages and solid lines and legends with suffix "c" denote averages over the regions with convective precipitation. Precipitation statistics from the CRM are included in (a), with the precipitation rates per rain event scaled to account for the difference in resolution between CRM and IFS.

the convection is already active during the strong moistening phase. Interestingly, the convective precipitation rate per event (solid lines in Fig. 6a) is minimum during the day in CTLc, while NEWc produces precipitation rates per event that peak at around 30 mm day^{-1} during late afternoon, which is more in line with the observed rain rates from mesoscale convective systems in the Sahel (Mathon et al. 2003). For comparison we have also plotted in Fig. 6a the total-area mean (dashed gray line) and resolution-scaled rainy-area mean precipitation (solid gray line) from the CRM, although data on the diurnal cycle from CRM also have to be interpreted with care (Langhans et al. 2012). The evolution of the total-area mean precipitation in the CRM during daytime is comparable to that of NEW, but it peaks 1–2 h later. Responsible for this shift is the growth in number and size of convective systems in the CRM during late afternoon and their tendency to produce more surface precipitation through reduced evaporation; these features are more difficult to represent with a diagnostic convection formulation. The CRM also produces more precipitation during the night, which is consistent with radar observations (Fig. 5). Interestingly, the onset of convection around 1200 LST, its average intensity, and its evolution during the afternoon (as measured by the rainy-area mean precipitation) compare reasonably well between NEW and the CRM. The low early morning rain rates in the CRM are related to boundary layer spinup processes (discussed later).

The low total-area mean precipitation rates in NEW in the late morning and early afternoon are the consequence

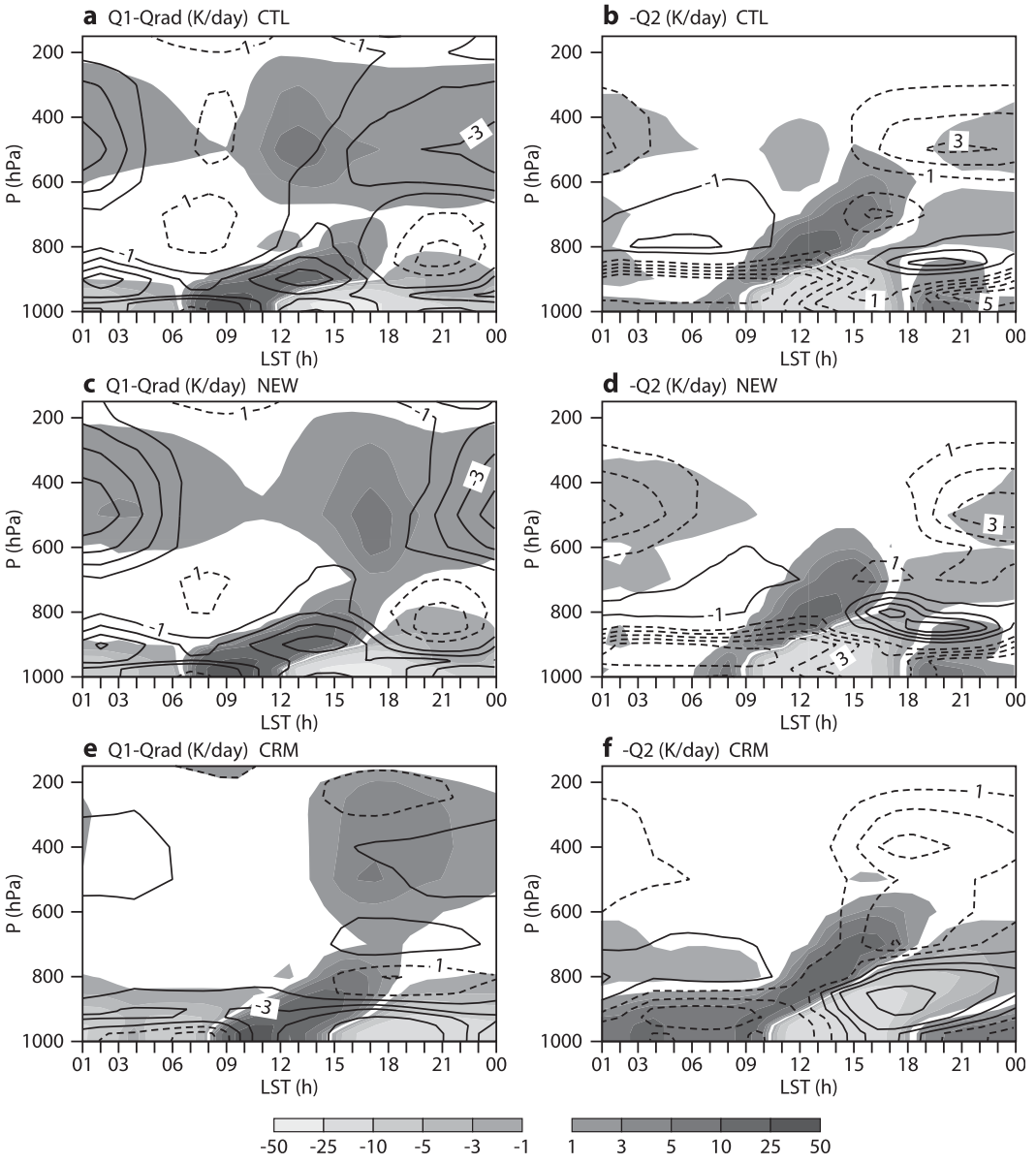

FIG. 7. Diurnal composites of heating and moistening rates (K day^{-1}) during 10–25 Jun 2012 over the central Sahel for (a),(b) CTL, (c),(d) NEW, and (e),(f) CRM. (left) Total heating rate minus radiation and (right) total moistening rate are shaded. Solid contour lines denote cooling and drying rates due to adiabatic motions; dashed contour lines (interval 1 K day^{-1}) denote adiabatic heating and moistening.

of low values of PCAPE′ in connection with long adjustment times and moderate subsidence stabilization (Figs. 6a,c–e). It will be illustrated in the next section that the resulting convective heating keeps the free troposphere in a marginal-stability regime. The increase in the convective adjustment time during late morning is produced by an increase in the cloud depth, while its decrease in the afternoon is caused by an increase in the mean updraft velocities. In conclusion, in nonstationary or nonequilibrium convection the various contributors to the forcing and stabilization interactively adjust. A successful simulation of the diurnal cycle requires most importantly a realistic formulation of the evolution of PCAPE′, which is dependent on the entrainment rates. The adjustment time scale in (12), which depends on PCAPE, is also an important factor for the representation of the spatial and temporal variability of convection.

b. Heating and moistening profiles

Composite diurnal cycles of the vertical distribution of the total heating rate (but excluding the radiative heating), and the total moistening rate, are illustrated in

Fig. 7. Using units of kelvins per day, these quantities are usually referred to as $Q_1 - Q_{rad}$ and $-Q_2$, respectively. The heating and moistening rates due to adiabatic motions have also been added as contours in Fig. 7 in order to distinguish convective and dynamical forcings.

One recognizes for both CTL and NEW (Figs. 7a,c) a distinctive phase with deep boundary layer heating from 0630 to 1200 LST, followed by boundary layer cooling and more elevated dry and shallow convective heating lasting until 1700 LST. Boundary layer moistening lasts until roughly 0900 LST, followed by strong drying of the lower boundary layer, and dry and shallow convective moistening of the lower troposphere extending to or exceeding the 600-hPa level at 1500–1600 LST. In both CTL and NEW, during the afternoon, there is also a strong drying by mean advection around 850 hPa that has also been noticed in observational studies (Zhang and Klein 2013). During the strong growth phase of the boundary layer from 1000 to 1700 LST, corresponding to a continuous growth of PCAPE′ in NEW (Fig. 6), the heating in the upper part of the boundary layer is in balance with the cooling due to adiabatic motions, but the upper troposphere is not in equilibrium. Indeed, the evolution of the upper-tropospheric heating profiles differs strongly between CTL and NEW. Whereas in CTL the mid- to upper-tropospheric heating of 5–10 K day^{-1} from precipitating deep convection occurs around 1300 LST, and therefore during the growth of the boundary layer, the strong deep convective heating in NEW occurs when the lower to middle troposphere has reached its maximum total heat content. Note that in NEW modest midtropospheric heating and therefore stabilization occur from around 1100 LST onward, and are due to cumulus congestus reaching heights of 500–400 hPa.

The dynamic response to deep convective heating is a couplet of upper-tropospheric cooling (lifting) and lower-tropospheric warming (subsidence) often called the stratiform mode. Through the quasigeostrophic adjustment process, it becomes effective a few hours after the convective heating. This dynamic cooling–heating couplet is particularly important for the formation of mesoscale stratiform rain during night. The upper-tropospheric response in NEW is clearly delayed and is stronger than that in CTL, attaining values of -4 K day^{-1}. Nevertheless, NEW still underestimates the nighttime precipitation with respect to the observations (Fig. 5).

A comparison of the heating and moistening profiles with CRM data (Figs. 7e,f) reveals that NEW produces a realistic diurnal cycle in phase and amplitude, including the shallow and congestus heating phase, although the latter is less pronounced in the CRM. The heating profiles (Figs. 7c,e) are also in fair agreement with the observed cloud evolution during days with late afternoon convection as reported by Zhang and Klein (2010). Interestingly, in both NEW and the CRM the maximum upper-tropospheric heating of up to 10 K day^{-1} occurs around 1700 LST. However, the heating peaks at higher altitudes in the CRM (400 hPa compared to 500 hPa in NEW), extends over a larger depth, and maintains its amplitude during the early night hours as does the surface precipitation. The moistening rates (Figs. 7d,f) are also in good agreement during daytime. However, larger differences in the heating profiles between the CRM and the IFS exist in the early morning hours which can be partly attributed to boundary layer spinup processes in the CRM.

The dynamic response to the convective heating is also comparable in structure and intensity between the CRM and NEW. The main difference is that the dynamical cooling is somewhat weaker in the CRM but occurs earlier (i.e., shortly after the maximum heating). The phase lag in the dynamical response between NEW and CRM becomes even more evident for the moistening profile (Fig. 7f). The reason for this phase difference is a tight coupling between resolved microphysics (condensation) and resolved dynamics (lifting) in the CRM, whereas with parameterized convection (a) Q_1 and Q_2 already contain a contribution from subgrid transport, and (b) the resolved flow has to adjust in response to a subgrid heat source. Furthermore, the dynamical drying in the CRM extends down to the surface between 1500 and 1800 LST when strong dynamical cooling also occurs. This dynamical feature is a signature of resolved downdrafts and cold pools in the CRM. Generally, we think that the structure and evolution of the convective heating and its dynamical response compare fairly between the CRM and NEW, given the limited domain size of the CRM and its sensitivity to the parameterization of horizontal mixing.

c. *Clouds and heating against satellite observations*

To further assess the structure and temporal evolution of the convective heating, the IFS has also been run in four-dimensional variational data assimilation (4D-Var) mode, permitting a better temporal and spatial evaluation against satellite data from geostationary infrared imagers and sun-synchronous microwave profilers.

A composite diurnal cycle of infrared brightness temperatures (BTs) in the 10.8-μm window has been computed in Fig. 8; it is representative for the Sahel for June–July 2012. The composites have been derived from two-dimensional probability density functions (PDFs) of BTs of the observed 1-hourly *Meteosat-9* images, and the BTs from synthetic satellite images from day-2

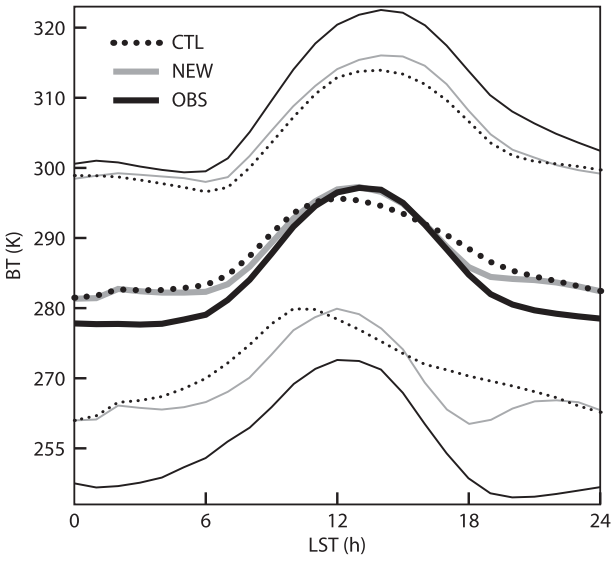

FIG. 8. Diurnal composite of mean and standard deviation of infrared BTs (K) in the 10.8-μm window during June–July 2012 over the central Sahel from *Meteosat-9*, and from the day-2 CTL and NEW forecasts. The composites have been computed from a two-dimensional PDF, and a −3-K bias correction has been applied to the forecasts. Thick lines correspond to median values, and thin lines correspond to plus or minus one standard deviation.

forecasts using the CTL and NEW; all data have been interpolated to a 0.4° grid. The observed BTs vary between 325 and 180 K, while the minima in the forecasts remain above 190 K. The forecast synthetic BTs have been bias corrected by −3 K, but there is still an important bias during the night corresponding to an underestimation of optically thick high clouds and nighttime precipitation, as already seen in Fig. 5. However, during the day the mean BTs from NEW closely follow the observed diurnal cycle, although the variability is still underestimated. In contrast, in the CTL, because of the occurrence of deep convection being too early, the BTs are too cold during noon and early afternoon, and too warm in the evening, where the variability is also strongly underestimated. The improved variability in NEW, and indeed better spatial representation of convection compared to CTL (not shown), is a consequence of the higher CAPE values and more realistic adjustment of the free troposphere. The interpretation of the improvement (cooler BTs) of NEW compared to CTL during the early morning hours is less obvious. Further investigation shows that this is caused by a combination of lower skin temperatures due to increased precipitation and soil moisture in the northern part of the domain, more residual elevated clouds from nighttime convection, and a more realistic convection in the tropical convergence zone extending into the southern part of the domain. All together, the results in Fig. 8 are consistent with the comparison against radar data given in Fig. 5.

Finally, a global picture of the improvement in the heating structure of NEW compared to CTL is given in Fig. 9 using July 2012 as an illustration. This shows a reduction in root-mean-square (rms) error of the BTs when evaluating the short-range (first guess) forecasts during the 12-h assimilation window against the clear-sky BTs from the Advanced Microwave Sounding Unit (AMSU)-A onboard sun-synchronous National Oceanic and Atmospheric Administration (NOAA) satellites. The satellites have different twice-daily overpass times, and the results are shown for two channels that are sensitive to temperatures over broad atmospheric layers around 500–1000 and 250–600 hPa. Clearly, NEW provides an improvement over CTL over most land regions with persistent active convection, and in particular in the middle to upper troposphere where the convective heating is strongest. The improvement of order 0.1 K is primarily a result of a reduction in the bias for the daytime overpasses. It is small in absolute values, but it is statistically significant, and has to be compared to the absolute rms error of the 12-h forecasts, which does not exceed 0.3 K. The areas of reduction in the short-range forecast errors are consistent with the improvements in the diurnal cycle seen in the long integrations (Fig. 2).

5. Conclusions

An entraining CAPE-dependent diagnostic closure for the cloud-base mass flux has been derived under the assumption of free-tropospheric quasi equilibrium that is subject to boundary layer forcing. The closure involves a convective adjustment time scale τ for the free troposphere that is proportional to the convective turnover time scale, and a coupling coefficient between the boundary layer and the free troposphere based on different time scales over land and water. With this formulation, only at the end of the lower-tropospheric heating and moistening cycle is the entire CAPE available to the convection.

The part of CAPE generation by boundary layer heating that is not available for consumption by deep convection motions is roughly proportional to the ratio α times the surface heat fluxes. Typical values of $0 \leq \alpha < 0.1$ reproduce the current model version CTL, which produces a diurnal cycle of convection over land that peaks around local noon. The NEW closure uses values of α over land in the range of $0.5 < \alpha \leq 1$. It is a pragmatic approach based on simple scaling arguments. This closure might numerically account for the gap between parcel theory (CAPE) and the ensemble-mean property (mass flux), but equivalent numerical results might in

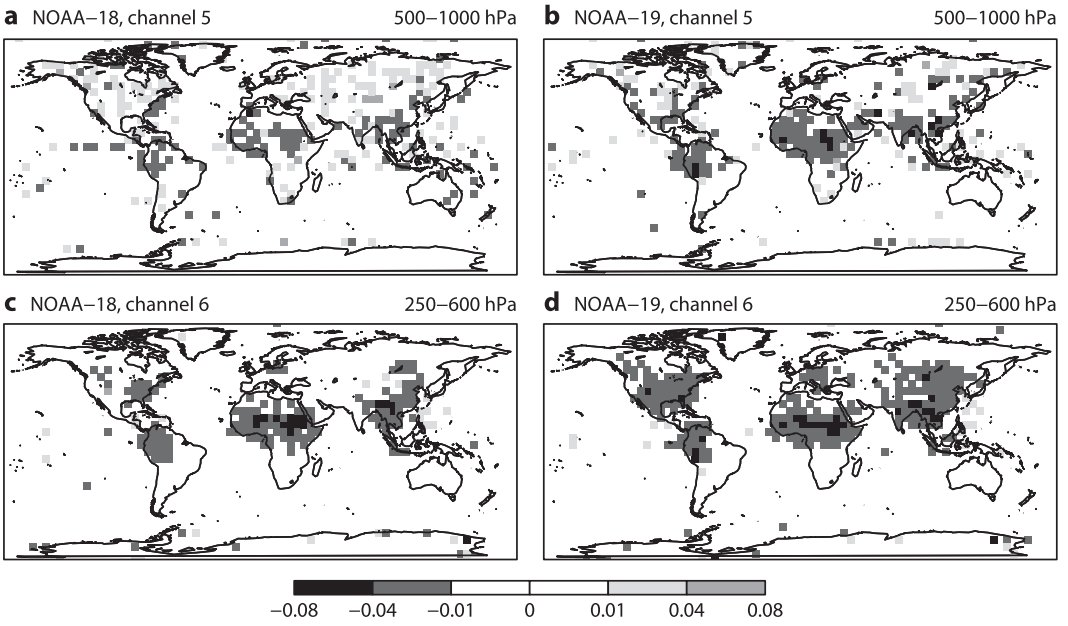

FIG. 9. Root-mean-square error differences in clear-sky BTs (K) for July 2012 between NEW and CTL during the 12-h window of the 4D-Var analysis, when evaluated against AMSU-A channels onboard NOAA sun-synchronous satellites. The channels are representative for different atmospheric layers: (a),(b) *NOAA-18* and *-19* channel 5 for the 500–1000-hPa layer, and (c),(d) *NOAA-18* and *-19* channel 6 for the 250–600-hPa layer. The twice-daily overpass times are 0300 and 1500 LST for *NOAA-18* and 0130 and 1330 LST for *NOAA-19*.

principle also be obtained with the aid of a (prognostic) plume ensemble. We do not yet know if this closure and the parameter range for α indeed reflect the actual physical coupling between the boundary layer and the deep convection (e.g., by implicitly accounting for the CIN/activation control where a shallow near-surface heating maximizes the effect on CIN), whereas a deep tropospheric anomaly maximizes the effect on CAPE (Mapes 2000; Parker 2002). It would be interesting to perform, in the parameterization context, further analyses of the coupling between the boundary layer and the deep convection based on observations and data from CRM, but this clearly is beyond our scope.

It has been shown through comparison with complementary data sources (e.g., radar data, and satellite data from infrared imager and microwave sounders) that NEW provides a fair representation of the observed daytime evolution of convection over land and increases its variability and intensity due to larger CAPE values in the afternoon. Furthermore, in NEW the shallow and congestus convection are present during the morning and early afternoon, respectively, while intense deep convection only sets in near the end of the lower- to midtropospheric heating and moistening cycle. This is in agreement with CRM data. The results are essentially independent of model resolution and time step. However, the current diagnostic formulation of convection with its diagnostic rain production is a limitation. We think that a further shift of the maximum precipitation by 1–2 h might be obtained by (a) coupling the convection to the stratiform prognostic microphysics not only via the condensate detrainment term, but also via precipitating species, or (b) using a more prognostic formulation of the convection.

A full verification and discussion of the impact of NEW on the general model performance is beyond the scope of the paper. As an illustrative example, Fig. 10 shows at a resolution of 0.2° the observed 10.8-μm infrared satellite image over Europe on 1 July 2012 and the synthetic forecast images from the $n = 1279$ ($\Delta x = 16$ km) 18-h forecasts. Indeed, NEW better represents the mainly surface-driven convection over the Balkans and the Atlas Mountains, a situation that can be frequently observed during summer. But compared to CTL, it also improves on the strongly synoptically forced convection over central Europe, where the timing of convection matters for the evolution of the mesoscale weather patterns. Further verification (not shown) confirms that the overall model performance, including the fit to wind data from soundings and profilers, is improved over the tropical land regions and the midlatitudes during summer. Notably, at 1800 LST near-surface temperatures are increased by 0.2–0.5 K, and boundary layer wind turning is increased. NEW has

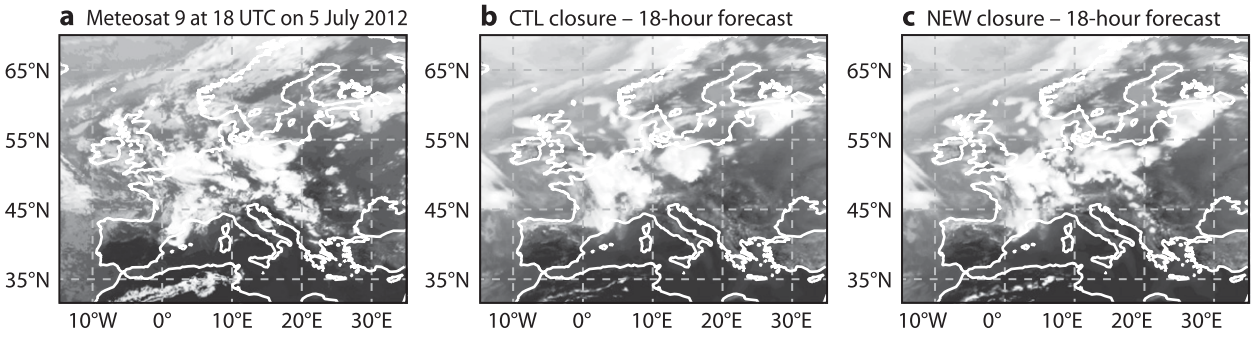

FIG. 10. Infrared 10.8-μm satellite image over Europe at 1800 UTC 5 Jun 2012 from (a) *Meteosat-9* channel 9, and from the 18-h forecasts at $n = 1279$ ($\Delta x = 16$ km) with (b) CTL and (c) NEW. All images are at resolution 0.2°.

become the operational version of the IFS as of November 2013.

So far, there has been little discussion on the effect of NEW over the oceans. In these areas, the overall synoptic impact can be described as largely neutral, including the medium-range forecasts of tropical cyclones and the representation of the Madden–Julian oscillation in seasonal integrations. However, there is a positive impact on the representation of convection and the diurnal cycle in near-coastal areas. Of particular concern in NWP is, for example, the inland advection of wintry showers forming over the relatively warm sea. This is illustrated by Fig. 11, which shows the 24-h precipitation accumulations over the British Isles and the near European mainland on 1 December 2010 as observed from ground-based radar along with the 24-h forecasts for

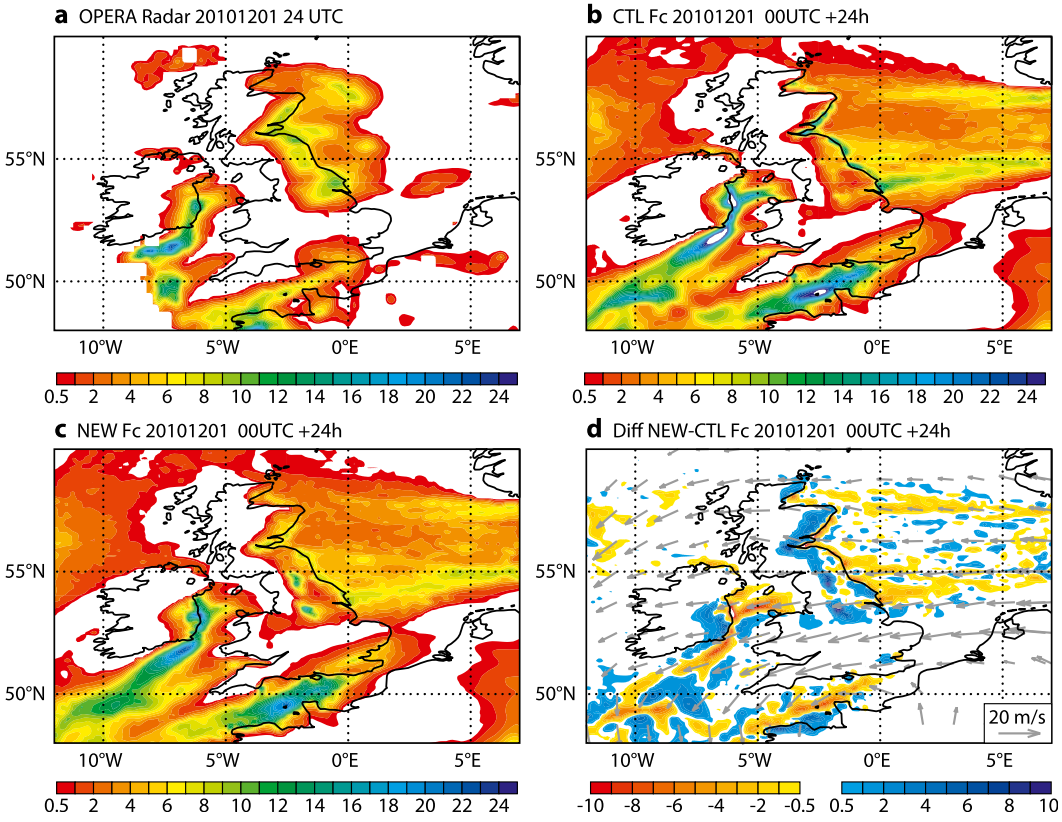

FIG. 11. 24-h precipitation accumulations (mm) for 1 Dec 2010 over the British Isles and near the European mainland from (a) radar observations on a 0.25° grid, and 24-h $n = 1279$ ($\Delta x = 16$ km) forecasts with (b) CTL, (c) NEW, and (d) difference between NEW and CTL. The advection is represented in (d) by the mean 500–850-hPa wind. NEW improves the RMSE against observations by 2% compared to CTL.

CTL and NEW with $n = 1279$. Nearly all precipitation accumulated as snow on the ground, reached up to 20 cm, and was predominantly of the convective type. Clearly, NEW reduces the unrealistically strong snowfall along the coast by up to 50% compared to CTL and more realistically moves the convective snowfall inland, bringing up an additional 10 cm of snow (Fig. 11d). This is possible even with a diagnostic formulation of convection as the moist unstable air is advected inland, and the simulated convection is formulated so that it is allowed to depart from elevated layers. The main difference between NEW and CTL is the slower convective adjustment, avoiding a too-strong large-scale response leading to coastal convergence. An improved version of CTL for this particular case could also be obtained by increasing the convective adjustment time. However, tests showed that this would significantly degrade the general model performance, highlighting again the need for a more flexible and dynamically targeted formulation of the convective adjustment in NWP.

Finally, concerning future higher-resolution upgrades of the IFS, from the current $n = 1279$ (16 km) operational resolution to the planned $n = 3999$ (5 km) resolution in 2020, we think that the convective closure described here will enable a smooth transition from parameterized to resolved deep convection as there is no longer a substantial discrepancy in the phase and location between parameterized and resolved convection. However, the intensity of the parameterized deep convection does not naturally diminish as resolution increases. For reasons of forecast performance (i.e., stronger stabilization with increasing forcing), the current adjustment time scale in (12) converges to the convective turnover time scale as resolution increases. One possible way of achieving vanishing parameterized tendencies for deep convection at high resolution is to increase the resolution-dependent factor $f(n)$ in (12) to infinity from some resolution onward, say $n = 2000$ (10 km). By doing so, the "small-area approximation" in the mass flux formulation is indirectly corrected for by a scaling, and the shape of the convective profiles is conserved. Instead, it might be necessary to recognize the limits of the small-area approximation more thoroughly and replace the grid-mean values in the computation of CAPE or PCAPE in (2) by the actual values in the environment.

Acknowledgments. The first author expresses his gratitude to Profs. Julia Slingo, Erland Källén, and Alan Thorpe for encouragements to never give up on the diurnal cycle. Two anonymous reviewers provided very helpful suggestions. We are also very grateful to Prof. Yukari Takayabu and her group at Tokyo University for providing the TRMM data, and to Dr. Peter Bauer for processing these data. Numerous discussions and critical evaluation of the model by our colleagues Drs. Irina Sandu, Richard Forbes, and Takuya Komori were extremely helpful, as was the assistance by Anabel Bowen in preparing the figures, and by Dr. Bob Riddaway in improving the text. We are grateful to the National Centers for Environmental Prediction (NCEP) for producing and the Joint Office for Science Support/University Corporation for Atmospheric Research (JOSS/UCAR) for providing the stage IV precipitation composites over the United States and thank Dr. Klaus Stephan from Deutsche Wetterdienst for providing the German radar precipitation composites. This work has also greatly benefited from the European Commission's COST action ES0905, and 7th Framework Programme EMBRACE project under Grant Agreement 282672.

APPENDIX

Entrainment and Detrainment Rates

a. Entrainment rates

Observations and CRMs show that midtropospheric relative humidity strongly controls the cloud-top heights (e.g., Derbyshire et al. 2004; Zhang and Klein 2010). A relative humidity (RH)-dependent entrainment parameterization is used that has been shown to reasonably fit CRM data (de Rooy et al. 2013) and allows a realistic reproduction of the large-scale convectively coupled waves in the tropics (Bechtold et al. 2008; Hirons et al. 2013b). The fractional updraft entrainment rate E^{up} (m^{-1}) for deep convection is parameterized as

$$E^{\mathrm{up}}_{\mathrm{deep}} = \varepsilon^{\mathrm{up}}(1.3 - \mathrm{RH})f_s,$$

$$\varepsilon^{\mathrm{up}} = 1.8 \times 10^{-3}\,\mathrm{m}^{-1}, \quad f_s = \left[\frac{q_{\mathrm{sat}}(\overline{T})}{q_{\mathrm{sat}}(\overline{T}_{\mathrm{base}})}\right]^3, \tag{A1}$$

where q_{sat} is the saturation specific humidity.

Entrainment above cloud base is applied to positively buoyant convection only. For shallow convection the entrainment rates are increased by a factor of 2, $E^{\mathrm{up}}_{\mathrm{shal}} = 2E^{\mathrm{up}}_{\mathrm{deep}}$, as also supported by CRM data. The vertical scaling function f_s in (A1) is supposed to mimic the effects of a cloud ensemble and the effect of the cloud diameter increasing with height. As the scaling function strongly decreases with height, the updraft detrainment rate (see below) will eventually become larger than the entrainment rate, and the mass flux starts to decrease with height.

Turbulent entrainment rates for the downdrafts are set to a constant value of $3 \times 10^{-4}\,\mathrm{m}^{-1}$. Downdraft organized entrainment is a function of buoyancy.

b. Detrainment rates

De Rooy et al. (2013) showed that detrainment rates can exhibit even larger variability than entrainment rates. A careful specification of detrainment rates is necessary to correctly simulate the moisture and momentum budget near detraining regions such as the trade inversion and the tropopause.

Turbulent detrainment rates (m^{-1}) for deep convection are also assumed to be RH dependent,

$$D^{\mathrm{up}}_{\mathrm{deep}} = \delta^{\mathrm{up}}(1.6 - \mathrm{RH}); \quad \delta^{\mathrm{up}} = 0.75 \times 10^{-4}\,\mathrm{m}^{-1}, \tag{A2}$$

whereas turbulent detrainment rates for shallow convection are set proportional to the entrainment rates:

$$D^{\mathrm{up}}_{\mathrm{shal}} = E^{\mathrm{up}}_{\mathrm{shal}}(1.6 - \mathrm{RH}). \tag{A3}$$

In addition, when the updraft becomes negatively buoyant, organized detrainment is applied. It is estimated by equating the decrease in updraft vertical kinetic energy at the top of the cloud to the decrease in mass flux with height.

Downdraft turbulent detrainments are set equal to the downdraft entrainment rates, while organized detrainment is enforced over the lowest 50 hPa.

REFERENCES

Ahlgrimm, M., and R. Forbes, 2012: The impact of low clouds on surface shortwave radiation in the ECMWF model. *Mon. Wea. Rev.,* **140,** 3783–3794.

Arakawa, A., and W. Schubert, 1974: Interaction of a cumulus cloud ensemble with the large-scale environment, Part I. *J. Atmos. Sci.,* **31,** 674–701.

Bechtold, P., J.-P. Chaboureau, A. Beljaars, A. K. Betts, M. Köhler, M. Miller, and J.-L. Redelsperger, 2004: The simulation of the diurnal cycle of convective precipitation over land in a global model. *Quart. J. Roy. Meteor. Soc.,* **130,** 3119–3137.

——, M. Köhler, T. Jung, F. Doblas-Reyes, M. Leutbecher, M. Rodwell, F. Vitart, and G. Balsamo, 2008: Advances in simulating atmospheric variability with the ECMWF model: From synoptic to decadal time-scales. *Quart. J. Roy. Meteor. Soc.,* **134,** 1337–1351.

Benedict, J. J., A. Sobel, D. M. W. Frierson, and L. J. Donner, 2013: Tropical intraseasonal variability in version 3 of the GFDL atmosphere model. *J. Climate,* **26,** 426–449.

Betts, A. K., and M. J. Miller, 1986: A new convective adjustment scheme. Part II: Single column tests using GATE wave, BOMEX, ATEX, and Arctic air-mass data sets. *Quart. J. Roy. Meteor. Soc.,* **112,** 693–710.

——, and C. Jakob, 2002: Study of diurnal cycle of convective precipitation over Amazonia using a single column model. *J. Geophys. Res.,* **107,** 4732, doi:10.1029/2002JD002264.

Blackburn, M., and Coauthors, 2013: The Aqua Planet Experiment (APE): CONTROL SST simulation. *J. Meteor. Soc. Japan,* **91A,** 17–56, doi:10.2151/jmsj.2013-A02.

Bougeault, P., 1985: A simple parameterization of the large-scale effects of cumulus convection. *Mon. Wea. Rev.,* **113,** 2108–2121.

Brockhaus, P., D. Lüthi, and C. Schär, 2008: Aspects of the diurnal cycle in a regional climate model. *Meteor. Z.,* **17,** 433–443.

Chaboureau, J.-P., F. Guichard, J.-L. Redelsperger, and J.-P. Lafore, 2004: The role of stability and moisture in the diurnal cycle of convection over land. *Quart. J. Roy. Meteor. Soc.,* **130,** 3105–3117.

Clark, A. J., W. A. Gallus Jr., and T.-C. Chen, 2007: Comparison of the diurnal precipitation cycle in convection-resolving and non-convection-resolving mesoscale models. *Mon. Wea. Rev.,* **135,** 3456–3473.

Craig, G. C., 1996: Dimensional analysis of a convecting atmosphere in equilibrium with external forcing. *Quart. J. Roy. Meteor. Soc.,* **122,** 1963–1967.

Dai, A., F. Giorgi, and K. E. Trenberth, 1999: Observed and model simulated diurnal cycles of precipitation over the contiguous United States. *J. Geophys. Res.,* **104,** 6377–6402.

Davies, L., R. S. Plant, and S. H. Derbyshire, 2013: Departures from convective equilibrium with a rapidly-varying surface forcing. *Quart. J. Roy. Meteor. Soc.,* **139,** 1731–1746, doi:10.1002/qj.2065.

Del Genio, A. D., and J. Wu, 2010: The role of entrainment in the diurnal cycle of continental convection. *J. Climate,* **23,** 2722–2738.

Derbyshire, S. H., I. Beau, P. Bechtold, J.-Y. Grandpeix, J.-M. Piriou, J.-L. Redelsperger, and P. M. M. Soares, 2004: Sensitivity of moist convection to environmental humidity. *Quart. J. Roy. Meteor. Soc.,* **130,** 3055–3079.

de Rooy, W., P. Bechtold, K. Fröhlich, C. Hohenegger, H. Jonker, S. Mironov, J. Teixeira, and J.-I. Yano, 2013: Entrainment and detrainment in cumulus convection: An overview. *Quart. J. Roy. Meteor. Soc.,* **139,** 1–19.

Donner, L. J., and V. T. Philips, 2003: Boundary-layer control on convective available potential energy: Implications for cumulus parametrization. *J. Geophys. Res.,* **108,** 4701, doi:10.1029/2003JD003773.

Emanuel, K. A., 1991: A scheme for representing cumulus convection in large scale models. *J. Atmos. Sci.,* **48,** 2313–2335.

——, 1993: The effect of convective response time on WISHE modes. *J. Atmos. Sci.,* **50,** 1763–1776.

——, J. D. Neelin, and C. S. Bretherton, 1994: On large-scale circulations in convecting atmospheres. *Quart. J. Roy. Meteor. Soc.,* **120,** 1111–1143.

Fletcher, J. K., and C. S. Bretherton, 2010: Evaluating boundary layer–based mass flux closures using cloud-resolving model simulations of deep convection. *J. Atmos. Sci.,* **67,** 2212–2225.

Fritsch, J. M., and C. G. Chappell, 1980: Numerical prediction of convectively driven mesoscale pressure systems. Part I: Convective parametrization. *J. Atmos. Sci.,* **37,** 1722–1733.

Fuchs, Z., and D. Raymond, 2007: A simple, vertically resolved model of tropical disturbances with a humidity closure. *Tellus,* **59A,** 344–354.

Gerard, L., J.-M. Piriou, R. Brozková, J.-F. Geleyn, and D. Banciu, 2009: Cloud and precipitation parameterization

in a meso-gamma-scale operational weather prediction model. *Mon. Wea. Rev.,* **137,** 3960–3977.

Grabowski, W. W., and Coauthors, 2006: Daytime convective development over land: an idealized model intercomparison based on LBA observations. *Quart. J. Roy. Meteor. Soc.,* **132,** 317–344.

Gregory, D., and P. R. Rowntree, 1990: A mass flux convection scheme with representation of cloud ensemble characteristics and stability-dependent closure. *Mon. Wea. Rev.,* **118,** 1483–1506.

——, J.-J. Morcrette, C. Jacob, A. C. M. Beljaars, and T. Stockdale, 2000: Revision of convection, radiation and cloud schemes in the ECMWF integrated forecasting system. *Quart. J. Roy. Meteor. Soc.,* **126,** 1685–1710.

Guichard, F., and Coauthors, 2004: Modelling the diurnal cycle of deep precipitating convection over land with CRMs and SCMs. *Quart. J. Roy. Meteor. Soc.,* **130,** 3139–3172.

Hirons, L., P. Inness, F. Vitart, and P. Bechtold, 2013a: Understanding advances in the simulation of intraseasonal variability in the ECMWF model. Part I: The representation of the MJO. *Quart. J. Roy. Meteor. Soc.,* **139,** 1417–1426, doi:10.1002/qj.2060.

——, ——, ——, and ——, 2013b: Understanding advances in the simulation of intraseasonal variability in the ECMWF model. Part II: The application of process-based diagnostics. *Quart. J. Roy. Meteor. Soc.,* **139,** 1427–1444, doi:10.1002/qj.2059.

Jones, T. R., and D. A. Randall, 2011: Quantifying the limits of convective parameterizations. *J. Geophys. Res.,* **106,** D08210, doi:10.1029/2010JD014913.

Jung, T., and Coauthors, 2010: The ECMWF model climate: Recent progress through improved physical parametrizations. *Quart. J. Roy. Meteor. Soc.,* **136,** 1145–1160.

Kain, J. S., and J. M. Fritsch, 1993: Convective parameterization for mesoscale models: The Kain–Fritsch scheme. *The Representation of Cumulus Convection in Numerical Models, Meteor. Monogr.,* No. 46, Amer. Meteor. Soc., 165–170.

Khairoutdinov, M., and D. A. Randall, 2006: High-resolution simulation of shallow-to-deep convection transition over land. *J. Atmos. Sci.,* **63,** 3421–3436.

Kim, D., A. H. Sobel, E. D. Maloney, D. M. W. Frierson, and L.-S. Kang, 2011: A systematic relationship between intraseasonal variability and mean state bias in AGCM simulations. *J. Climate,* **24,** 5506–5520.

Lafore, J.-P., and Coauthors, 1998: The Meso-NH Atmospheric Simulation System. Part I: Adiabatic formulation and control simulations. Scientific objectives and experimental design. *Ann. Geophys.,* **16,** 90–109.

Langhans, W., J. Schmidli, and C. Schär, 2012: Bulk convergence of cloud-resolving simulations of moist convection over complex terrain. *J. Atmos. Sci.,* **69,** 2207–2228.

——, ——, O. Fuhrer, S. Bieri, and C. Schär, 2013: Long-term simulations of thermally-driven flows and orographic convection at convection-parameterizing and cloud-resolving resolutions. *J. Appl. Meteor. Climatol.,* **52,** 1490–1510.

Lin, J.-L., and Coauthors, 2006: Tropical intraseasonal variability in 14 IPCC AR4 climate models. Part I: Convective signals. *J. Climate,* **19,** 2665–2690.

Lin, Y., and K. E. Mitchell, 2005: The NCEP stage II/IV hourly precipitation analyses: Development and applications. *Extended Abstracts, 19th Conf. on Hydrology,* San Diego, CA, Amer. Meteor. Soc., 1.2. [Available online at https://ams.confex.com/ams/Annual2005/techprogram/paper_83847.htm.]

——, and Coauthors, 2012: TWP-ICE global atmospheric model intercomparison: Convection responsiveness and resolution impact. *J. Geophys. Res.,* **117,** D09111, doi:10.1029/2011JD017018.

Mapes, B. E., 2000: Convective inhibition, subgrid-scale triggering energy, and stratiform instability in a toy tropical wave model measurements. *J. Atmos. Sci.,* **57,** 1515–1535.

Marsham, J. H., N. Dixon, L. Garcia-Carreras, G. M. S. Lister, P. Knippertz, and C. Birch, 2013: The role of moist convection in the West African monsoon system: Insights from continental-scale convection-permitting simulations. *Geophys. Res. Lett.,* **40,** 1843–1849, doi:10.1002/grl.50347.

Mathon, V., H. Laurent, and T. Lebel, 2003: Mesoscale convective system rainfall in the Sahel. *J. Appl. Meteor. Climatol.,* **41,** 1081–1092.

Neelin, J. D., and J.-Y. Yu, 1994: Modes of tropical variability under convective adjustment and the Madden–Julian oscillation. Part I: Analytical theory. *J. Atmos. Sci.,* **51,** 1876–1894.

Nesbitt, S. W., and E. J. Zipser, 2003: The diurnal cycle of rainfall and convective intensity according to three years of TRMM measurements. *J. Climate,* **16,** 1456–1475.

Nordeng, T.-E., 1994: Extended versions of the convection parametrization scheme at ECMWF and their impact upon the mean climate and transient activity of the model in the tropics. ECMWF Tech. Memo. 206, 41 pp.

Pan, D.-M., and D. A. Randall, 1998: A cumulus parameterization with prognostic closure. *Quart. J. Roy. Meteor. Soc.,* **124,** 949–981.

Parker, D. J., 2002: The response of CAPE and CIN to tropospheric thermal variations. *Quart. J. Roy. Meteor. Soc.,* **128,** 119–130.

Petch, J. C., A. R. Brown, and M. E. B. Gray, 2002: The impact of horizontal resolution on the simulations of convective development over land. *Quart. J. Roy. Meteor. Soc.,* **28,** 2031–2044.

Piriou, J.-M., J.-L. Redelsperger, J.-F. Geleyn, J.-P. Lafore, and F. Guichard, 2007: An approach for convective parameterization with memory, in separating microphysics and transport in grid-scale equations. *J. Atmos. Sci.,* **64,** 4127–4139.

Raymond, D. J., 1995: Regulation of moist convection over the west Pacific warm pool. *J. Atmos. Sci.,* **52,** 3945–3959.

——, and M. J. Herman, 2011: Convective quasi-equilibrium reconsidered. *J. Adv. Model. Earth Syst.,* **3,** M08003, doi:10.1029/2011MS000079.

Rio, C., F. Hourdin, J.-Y. Grandpeix, and J. P. Lafore, 2009: Shifting the diurnal cycle of parameterized deep convection over land. *Geophys. Res. Lett.,* **36,** L07809, doi:10.1029/2008GL036779.

Sato, T., T. Yoshikane, M. Satoh, H. Miura, and H. Fujinami, 2008: Resolution dependency of the diurnal cycle of convective clouds over the Tibetan Plateau in a mesoscale model. *J. Meteor. Soc. Japan,* **86A,** 17–31.

——, H. Miura, M. Satoh, Y. N. Takayabu, and Y. Wang, 2009: Diurnal cycle of precipitation in the tropics simulated in a global cloud-resolving model. *J. Climate,* **22,** 4809–4826.

Schlemmer, L., C. Hohenegger, J. Schmidli, C. Bretherton, and C. Schär, 2011: An idealized cloud-resolving framework for the study of summertime midlatitude diurnal convection over land. *Quart. J. Roy. Meteor. Soc.,* **68,** 1041–1057.

Shutts, G. J., and M. E. B. Gray, 1999: Numerical simulations of convective equilibrium under prescribed forcing. *Quart. J. Roy. Meteor. Soc.,* **125,** 2767–2787.

Slingo, J. M., K. Sperber, J.-J. Morcrette, and G. L. Potter, 1992: Analysis of the temporal behavior of convection in the tropics

of the European Centre for Medium-Range Weather Forecasts model. *J. Geophys. Res.,* **97,** 18 119–18 135.

Stirling, A., and R. A. Stratton, 2012: Entrainment processes in the diurnal cycle of deep convection over land. *Quart. J. Roy. Meteor. Soc.,* **138,** 1135–1149.

Stratton, R. A., and A. Stirling, 2012: Improving the diurnal cycle of convection in GCMs. *Quart. J. Roy. Meteor. Soc.,* **138,** 1121–1134.

Takayabu, Y., and M. Kimoto, 2008: Diurnal march of rainfall simulated in a T106 AGCM and dependence on cumulus schemes. *J. Meteor. Soc. Japan,* **86A,** 163–173.

Tian, B., I. M. Held, N.-C. Lau, and B. J. Soden, 2005: Diurnal cycle of summertime deep convection over North America: A satellite perspective. *J. Geophys. Res.,* **110,** D08108, doi:10.1029/2004JD005275.

Tiedtke, M., 1989: A comprehensive mass flux scheme for cumulus parametrization in large-scale models. *Mon. Wea. Rev.,* **117,** 1779–1800.

Vitart, F., and F. Molteni, 2010: Simulation of the Madden–Julian oscillation and its teleconnections in the ECMWF forecast system. *Quart. J. Roy. Meteor. Soc.,* **136,** 842–856.

Yang, G.-Y., and J. Slingo, 2001: The diurnal cycle in the tropics. *Mon. Wea. Rev.,* **129,** 784–801.

Yano, J.-I., and R. Plant, 2012: Finite departures from convective quasi-equilibrium: Periodic cycle and discharge–recharge mechanism. *Quart. J. Roy. Meteor. Soc.,* **138,** 626–637.

——, M. Bister, Z. Fuchs, L. Gerard, V. Phillips, S. Barkidija, and J.-M. Piriou, 2013: Phenomenology of convection-parameterization closure. *Atmos. Chem. Phys.,* **13,** 1411–4131, doi:10.5194/acp-13-4111-2013.

Zhang, G. J., 2002: Convective quasi-equilibrium in midlatitude continental environment and its effect on convective parameterization. *J. Geophys. Res.,* **107** (D14), doi:10.1029/2001JD001005.

——, and N. A. McFarlane, 1995: Sensitivity of climate simulations to the parameterization of cumulus convection in the Canadian Climate Centre general circulation model. *Atmos.–Ocean,* **33,** 407–446.

Zhang, Y., and S. A. Klein, 2010: Mechanisms affecting the transition from shallow to deep convection over land: Interferences from observations of the diurnal cycle collected at the ARM Southern Great Plains site. *J. Atmos. Sci.,* **67,** 2943–2959.

——, and ——, 2013: Factors controlling the vertical extent of fair-weather shallow cumulus clouds over land: Investigation of diurnal-cycle observations collected at the ARM Southern Great Plains site. *J. Atmos. Sci.,* **70,** 1297–1315.

Zimmer, M., G. C. Craig, C. Keil, and H. Wernli, 2011: Classification of precipitation events with a convective response timescale and their forecasting characteristics. *Geophys. Res. Lett.,* **38,** L05802, doi:10.1029/2010GL046199.